

Modeling of Advanced Melting Zone for Manufacturing of Optical Fibers*

Zhiyong Wei

e-mail: gte384w@prism.gatech.edu

Kok-Meng Lee

kokmeng.lee@me.gatech.edu

The George W. Woodruff School of Mechanical Engineering,
Georgia Institute of Technology,
Atlanta, GA 30332-0405

Zhi Zhou

e-mail: zhizhou@ofsoptics.com

Siu-Ping Hong

e-mail: shong@ofsoptics.com

OFS
Norcross, GA 30071

Optical fibers are drawn from preforms (fused silica glass rods) typically made up of two concentric cylinders (the core rod and the clad tube), which are usually joined in a separate fusion process. The setup time and hence manufacturing cost can be significantly reduced if the two cylinders can be joined in the same furnace in which the fiber is drawn. A good understanding of the transient temperature distribution is needed for controlling the feed rate to avoid thermally induced cracks. Since direct measurement of the temperature fields is often impossible, the geometrical design of the preform and the control of the feed rate have largely been accomplished by trials-and-errors. The ability to predict the transient temperature distribution and the thermally induced stresses will provide a rational basis to design optimization and feed rate control of the process. In this paper, we present an analytical model to predict the transient conductive-radiative transfer as two partially joined, concentric glass cylinders with specular surfaces are fed into the furnace. Finite volume method (FVM) is used to solve the radiative transfer equation (RTE). The specular surface reflectivity is obtained by the Fresnel's law and the Snell's law. The boundary intensities are obtained through the coupling of the interior glass radiative transfer and the exterior furnace enclosure analysis. The model has been used to numerically study the transient conductive-radiative transfer in the advanced melting zone (AMZ) of an optic fiber drawing process. This problem is of both theoretical and practical interest in the manufacture of optical fibers. The computational method for the radiation transfer developed in this paper can also be applied to the simulation of the fiber drawing process and other glass-related manufacturing processes. [DOI: 10.1115/1.1751426]

1 Introduction

Optical fibers are drawn from preforms (melting fused silica glass rods) typically made up of two concentric cylinders (the core and the cladding) in a furnace operating at a temperature near the glass melting point (between 1500 K to 2500 K). The core and the cladding are usually joined in a separate (preheating) fusion process that is typically carried out manually. To minimize the setup time and thus lower the manufacturing cost, it is desired to eliminate this time-consuming fusion process by advancing the two cylinders (initially at room temperature) at a predetermined feed rate into the same furnace that the fiber is drawn. The tradeoff is that sophisticated feed rate control is needed to avoid large temperature gradient in the advanced melting zone (AMZ), which could result in cracking at the interface before the glass cylinder is softened. As direct measurement of the temperature fields and thermal stresses is often impossible, the geometrical design of the preform and the control of the feed rate have largely been accomplished by trials-and-errors. The ability to predict the transient temperature distribution and the thermally induced stresses will provide a rational basis to design optimization and feed rate control of the process.

Radiation is the dominant heat transfer mode in this process due to the high temperature of the furnace. Because glass is semitransparent to radiation, emission and absorption exist throughout the medium. A number of researchers (Paek and Runk [1], Myers [2], Xiao and Kaminski [3], Choudhury et al. [4]) have used Rosseland's approximation, which assumes the participating medium is optically thick, to model the radiative transport in the steady state fiber drawing process that follows the AMZ process. Lee and

Viskanta [5] investigated combined conduction and radiation in a one-dimensional glass layer. By comparing the results from the exact integral solution and the Rosseland approximation method, they concluded that the diffusion approximation greatly underestimates the temperature and heat flux when the thickness or the opacity of the layer is small.

Recently, the finite volume method (FVM) has been investigated for modeling semitransparent, emitting and absorbing medium. The method has a flexibility to lay out the spatial and angular grids and can solve the radiative transfer equation (RTE) numerically without any assumption. Chai et al. [6] presented the procedure of the FVM and tested the method with benchmark problems of two- and three-dimensional enclosures with participating media. The results demonstrated that the method is accurate and efficient when compared with the exact solution or discrete ordinates method (DOM). Liu et al. [7] compared the FVM and the DOM on benchmark problems in body-fitted coordinates of Cartesian geometry. Their results from both methods show reasonably good agreements and in some cases, the FVM outperforms the DOM. Baek and Kim [8] presented the FVM in an axisymmetric cylindrical geometry and obtained accurate solution for benchmark problems. Most of the studies in these problems have relatively simple boundary conditions, either a bounding opaque wall or an environment with a uniform temperature.

The solution of the RTE requires well defined boundary intensities at all the interfaces. The optical condition of the interfaces has significant effects on the radiative transfer through the surfaces. In the prior works on the fiber drawing simulation, Yin and Jaluria [9], Siegel and Spuckler [10] assumed the interfaces of the preform are diffuse to irradiations when the preform has not been polished. It is of interest to investigate the effect of surface conditions on the solution of the RTE since most preforms made through the modified chemical vapor deposition (MCVD) process are optically smooth. For an ideally smooth surface, Snell's law and Fresnel's law can be used to calculate the reflectivities of the

Contributed by the Manufacturing Engineering Division for publication in the JOURNAL OF MANUFACTURING SCIENCE AND ENGINEERING. Manuscript received Nov. 2002; Revised Nov. 2003. Associate Editor: R. E. Smelser.

*This paper was previously published in 126(2) May 2004 with incorrect figures. We are republishing it with the correct figures.

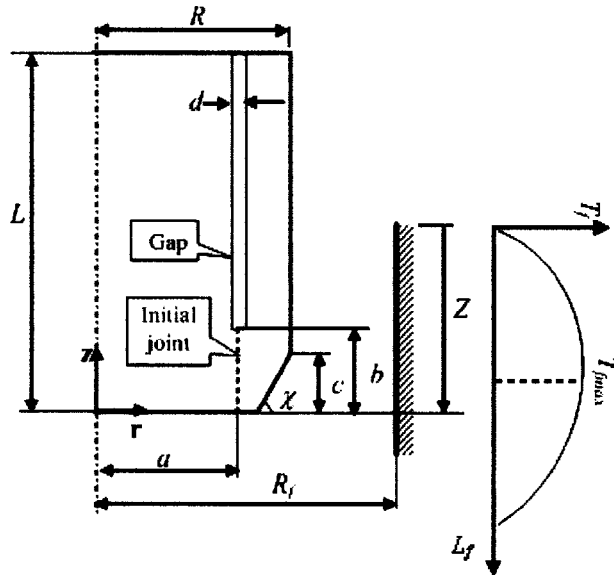


Fig. 1 Schematic illustrating the transient process

surface (Lee and Viskanta [5]). Since the boundary intensities and the reflectivities depend on directions at specular surfaces, denser angular grids are required at the surfaces in order to address the direction tracing of each reflection and refraction.

In this paper, we use the FVM to predict the transient conductive-radiative transfer as two partially joined, concentric glass cylinders with specular surfaces are moved into the furnace. The numerical model provides an effective means to predict and visualize the temperature field, upon which practical methods for reducing the transient temperature gradient (and thus the thermal crack) can be developed. The computational method for radiation transfer developed here can also be applied to the simulation of the fiber drawing process and other glass-related manufacturing processes.

2 Heat Transfer Model of the Advanced Melting Zone (AMZ)

The geometry of the thermal system characterizing the AMZ is shown in Fig. 1. The thermal system is axisymmetric and two-dimensional (2D). As shown in Fig. 1, the system consists of a cylindrical furnace that has a parabolic temperature distribution with a maximum at the middle, and a fused silica assembly. The glass assembly (called preform in industry) is made up of a core rod and a clad tube of radii a and R respectively, where the gap d between the two concentric cylinders is very small as compared to the radii. The cylinders are initially joined for a short length b at the bottom. The cladding tube has a taper (angle χ) at the bottom. The preform (initially at room temperature) is translated axially into the furnace till the lower end of the rod reaches the middle of the furnace, where the gap is sealed under heat. In the following analysis, the symbols for the parameters and variables are defined in the nomenclature.

The rate of change of energy stored in a glass element is contributed by both conductive and radiative transfer as characterized by the heat equation:

$$\rho C \frac{\partial T}{\partial t} = -\nabla \cdot (-k \nabla T) - \nabla \cdot \mathbf{q} \quad (1)$$

In Eq. (1), the divergence of the total radiation heat flux is given by (Modest, [11]):

$$\nabla \cdot \mathbf{q} = \int_0^\infty \left[4\pi \kappa_\lambda n_\lambda^2 I_{b\lambda}(T) - \kappa_\lambda \int_{\Omega=4\pi} I_\lambda(\mathbf{r}, \mathbf{s}) d\Omega \right] d\lambda \quad (2)$$

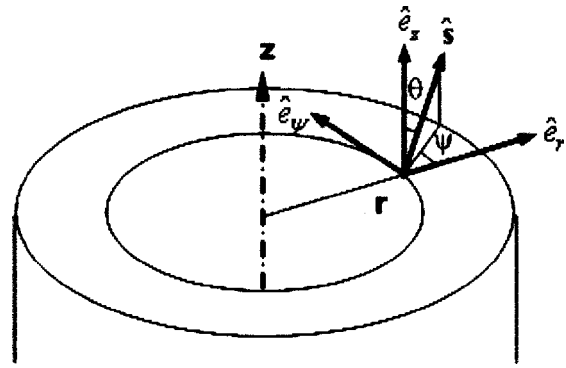


Fig. 2 Local orientation coordinate system in the 2D axisymmetric cylindrical system

When scattering of radiation is negligible as compared to the absorption and the emission (Viskanta [12]), the radiation intensity $I_\lambda(\mathbf{r}, \mathbf{s})$ in Eq. (2) can be solved from the radiative transfer equation (RTE):

$$\mathbf{s} \cdot \nabla I_\lambda(\mathbf{r}, \mathbf{s}) = \kappa_\lambda [n_\lambda^2 I_{b\lambda}(T) - I_\lambda(\mathbf{r}, \mathbf{s})] \quad (3)$$

As the natural convection of the air is negligible in comparison to the radiative exchange, the boundary condition for the heat equation is essentially the continuity of the conductive heat flux and the net radiative flux at the opaque band given as follows:

$$-k \mathbf{n} \cdot \nabla T = q_{rad, opa} \quad (4)$$

Equations (1) to (4) are solved numerically for the transient temperature distribution in the AMZ. Specifically, the heat equation or Eq. (1) can be solved by using the standard spatial FVM with a semi-implicit time-marching scheme. However, the solution to Eq. (1) requires solving the RTE, the closed form solution for which is not available. Thus, the RTE is solved numerically in the following subsections.

2.1 Radiative Transfer Computation. The following assumptions are made in solving the RTE: (a) Glass is semitransparent in the spectral range $0 < \lambda < 5 \mu\text{m}$ and is almost opaque beyond $5 \mu\text{m}$. (b) The refractive index of the medium is uniform and does not depend on temperature in the range considered. (c) The furnace walls are gray and diffuse. (d) The inner and outer surfaces at the glass interface and in the gap are optically smooth for radiation reflection and transmission. (e) The glass has not melted during transient, and the effects of the small deformation of the glass rod on the surface reflection and transmission is negligible.

To allow for axi-symmetric but arbitrary non-uniform cross-section, the RTE or Eq. (3) is transformed in a cylindrical curvilinear coordinate system (η, ξ) in the strong conservative form:

$$\begin{aligned} \frac{\partial}{\partial \eta} \left[r I_\lambda \left(\frac{\alpha \eta_r + \beta \eta_z}{J} \right) \right] + \frac{\partial}{\partial \xi} \left[r I_\lambda \left(\frac{\alpha \xi_r + \beta \xi_z}{J} \right) \right] - \frac{1}{J} \frac{\partial}{\partial \psi} (\gamma I_\lambda) \\ = \frac{r \kappa_\lambda}{J} (I_{b\lambda} - I_\lambda) \end{aligned} \quad (5)$$

where $(\alpha = \sin \theta \cos \psi, \gamma = \sin \theta \sin \psi, \beta = \cos \theta)$ are the direction cosines of the intensity orientation vector \mathbf{s} (see Fig. 2); (η_r, η_z) and (ξ_r, ξ_z) are the grid metrics; and J is the Jacobian of the transform. The derivation of Eq. (5) is attached in the appendix. From now on we drop the subscript λ for convenience, but it should be kept in mind that the intensities and the median radiation properties are all spectral values and are evaluated in different bands of the spectrum.

The RTE is solved using the FVM. The method involves dividing the 2D spatial domain into finite control volumes, each of which has a local orientation coordinate system as shown in Fig.

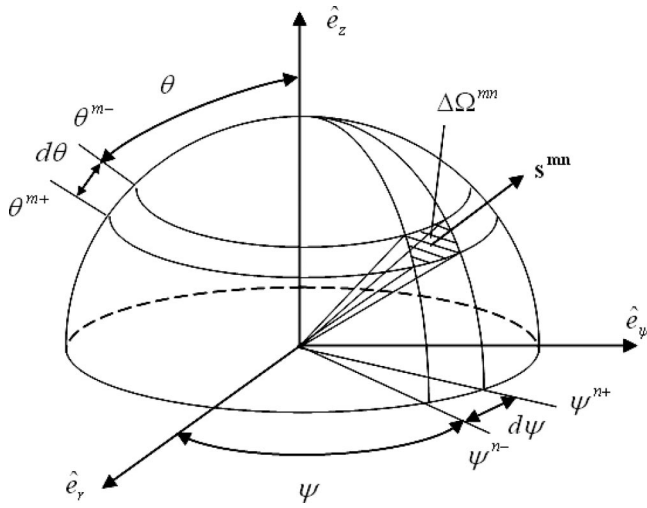


Fig. 3 Representative control solid angle in the local coordinate system

2. The whole solid angle space in each local coordinate system is further divided into finite control angles as shown in Fig. 3. The control angle is defined by $\Delta\Omega^{mn} = \int_{\psi^{m-}}^{\psi^{m+}} \int_{\theta^{m-}}^{\theta^{m+}} \sin\theta d\theta d\psi$. The RTE is then solved along each direction of the control angle in each control volume. The advantage of the FVM is that the control angles can be arbitrarily specified pertaining to each problem dealt with. Equation (5) is spatially discretized by central difference and then integrated over each of the control angles, which leads to

$$\sum_{i=e,n} I_i^{mn} D_i^{mn} - \sum_{i=w,s} I_i^{mn} D_i^{mn} - \frac{1}{J} (a^{m,n+1/2} I_p^{m,n+1/2} - a^{m,n-1/2} I_p^{m,n-1/2}) = \frac{rK}{J} (I_b - I_p^{mn}) \Delta\Omega^{mn} \quad (6)$$

where the superscripts m and n denote the discrete polar and azimuthal angles of \mathbf{s} ; $m=1,2,\dots,M$; $n=1,2,\dots,N$; e, n, w and s denote the east, north, west and south faces of the control volume; and the subscript "p" denotes the center node of the control volume. In Eq. (6), $D_i^{mn} = r_i \int_{\Delta\Omega^{mn}} \mathbf{A}_i \cdot \mathbf{s} d\Omega$ is the face intensity weight given by

$$D_i^{mn} = \begin{cases} \frac{r_i}{J_i} (\eta_{ri} D_{cr}^{mn} + \eta_{zi} D_{cz}^{mn}) & \text{for } i=e,w \\ \frac{r_i}{J_i} (\xi_{ri} D_{cr}^{mn} + \xi_{zi} D_{cz}^{mn}) & \text{for } i=s,n \end{cases} \quad (7)$$

where

$$D_{cr}^{mn} = \int_{\psi^{m-}}^{\psi^{m+}} \int_{\theta^{m-}}^{\theta^{m+}} (\sin\theta \cos\psi) \sin\theta d\theta d\psi \quad (8)$$

$$D_{cz}^{mn} = \int_{\psi^{m-}}^{\psi^{m+}} \int_{\theta^{m-}}^{\theta^{m+}} \cos\theta \sin\theta d\theta d\psi \quad (9)$$

Since $a^{mn \pm 1/2}$ are the geometric coefficients for the intensities on the faces of the control angle, they do not depend on the intensities. The following recursive relation can be obtained by assuming all the facial and nodal intensities in Eq. (6) are equal to the blackbody emission intensity:

$$a^{m,n+1/2} - a^{m,n-1/2} = J \left(\sum_{i=e,n} D_i^{mn} - \sum_{i=w,s} D_i^{mn} \right) = D_{cr}^{mn} \quad (10)$$

subject to the boundary condition $a^{m,N+1/2} = 0$.

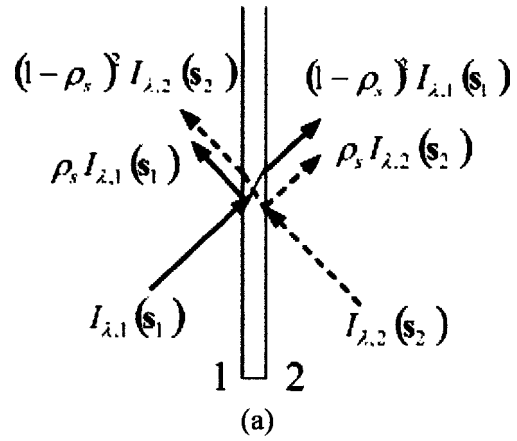


Fig. 4 Schematics illustrating the boundary conditions: (a) Gap between the two cylinders; (b) Interface of the glass rod

Since $I_{e,w,s,n}^{mn}$ and $I_p^{m,n \pm 1/2}$ appear in Eq. (6), supplementary relationships between these intensities and the nodal intensity I_p^{mn} are required to solve the discretized equation. In order to ensure positive intensity solution, the step scheme (Baek and Kim [8]) is used to relate the facial and edge intensities to the nodal intensity.

2.2 Boundary Conditions for the RTE and the Enclosure Analysis. The solution of the RTE requires an appropriate set of boundary intensities that start from all the inner surfaces of the glass media and at the symmetry axis. Along the axis of the symmetry, or at

$$r=0 \quad I'_\lambda = I_\lambda \quad \text{for } \beta' = \beta \quad \text{and} \quad \alpha' = -\alpha \quad (11)$$

where I'_λ is along the reflection direction of an incident intensity I_λ .

For optically smooth glass, the direction of the refracted intensity at a surface follows the Snell's law:

$$n_1 \sin\theta_1 = n_2 \sin\theta_2 \quad (12)$$

where n is the index of refraction; θ is the angle between the intensity and the normal vector of the surface; and the subscripts 1 and 2 represent either the glass or the air media. The reflectivity from media 1 to media 2 at the interface can be obtained by the Fresnel's law:

$$\rho_{1-2} = \frac{1}{2} \left[\left(\frac{n_1 \cos\theta_2 - n_2 \cos\theta_1}{n_1 \cos\theta_2 + n_2 \cos\theta_1} \right)^2 + \left(\frac{n_1 \cos\theta_1 - n_2 \cos\theta_2}{n_1 \cos\theta_1 + n_2 \cos\theta_2} \right)^2 \right] \quad (13)$$

where $\rho_{1-2}(\theta_1) = \rho_{2-1}(\theta_2)$ and thus we use $\rho_s(\theta)$ to represent the specular reflectivity.

Figures 4(a) and 4(b) illustrate the transmission and reflection at the gap between the cylinders and at the surface respectively. In Fig. 4(a), $I_{\lambda,1}(\mathbf{s}_1)$ and $I_{\lambda,2}(\mathbf{s}_2)$ are the incident radiation intensities onto the gap from within the glass media. Consider the multiple reflections between the two outer surfaces at the gap. The boundary intensities leaving the inner surfaces 1 and 2 at the gap and pointing toward the interior of the glass media can be obtained by

$$I_{\lambda,i}^B(\mathbf{r}, \mathbf{s}'_i) = \left[1 + \frac{(1-\rho_s(\theta))^2}{1-\rho_s^2(\theta)} \right] \rho_s(\theta) I_{\lambda,i}(\mathbf{r}, \mathbf{s}_i) + \frac{(1-\rho_s(\theta))^2}{1-\rho_s^2(\theta)} I_{\lambda,j}(\mathbf{r}, \mathbf{s}_j) \quad i,j=1,2 \quad (14)$$

where \mathbf{s}'_i is along the reflection direction of the incident intensity $I_{\lambda,i}(\mathbf{r}, \mathbf{s}_i)$.

Figure 4(b) illustrates the boundary conditions for two separate bands. In the semitransparent band ($0 < \lambda < 5 \mu\text{m}$), $I_{\lambda,f}(\mathbf{s}_f)$ and

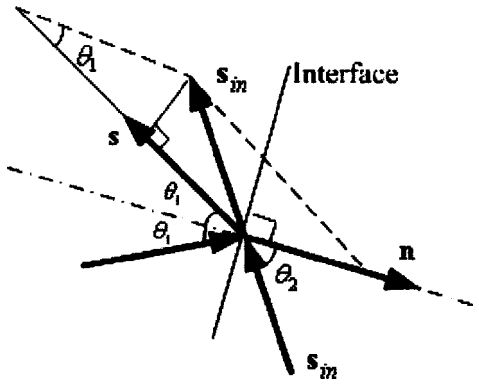


Fig. 5 Determination of the incident intensity unit vectors \mathbf{s}_f and \mathbf{s}_g

$I_{\lambda,g}(\mathbf{s}_g)$ are the incident radiation intensity from the furnace wall and from within the glass media. The boundary intensity leaving the inner surface and pointing to the glass interior is made up of the transmission of $I_{\lambda,f}(\mathbf{s}_f)$ and the reflection of $I_{\lambda,g}(\mathbf{s}_g)$.

$$I_{\lambda}^R(\mathbf{r}, \mathbf{s}'_g) = [1 - \rho_s(\theta)](n_g/n_a)^2 I_{\lambda,f}(\mathbf{r}_f, \mathbf{s}_f) + \rho_s(\theta) I_{\lambda,g}(\mathbf{r}, \mathbf{s}_g) \quad \text{for } \mathbf{n} \cdot \mathbf{s}'_g < 0 \quad (15)$$

where \mathbf{s}'_g is along the reflection direction of the incident intensity $I_{\lambda,g}(\mathbf{s}_g)$, and \mathbf{n} is the outward unit normal vector at the glass surface. Note that the transmitted intensity is multiplied by a factor of $(n_2/n_1)^2$ for a transmission from media 1 to media 2 due to the change of the solid angle caused by the refraction.

Based on the geometric relationships among the direction vectors at the glass surface as shown in Fig. 5, the angles between the intensities and the unit normal vector and the incident intensity orientation unit vectors are determined by

$$\theta_1 = \cos^{-1}(-\mathbf{n} \cdot \mathbf{s}'_g), \quad \theta_2 = \sin^{-1}[(n_g/n_a)\sin(\theta_1)]$$

$$\mathbf{s}_g = \mathbf{s}'_g - 2(\mathbf{n} \cdot \mathbf{s}'_g)\mathbf{n} \quad (16)$$

$$\mathbf{s}_f = \left[\cos(\theta_2 - \theta_1) + \frac{\sin(\theta_2 - \theta_1)}{\tan(\theta_1)} \right] \mathbf{s}'_g + \frac{\sin(\theta_2 - \theta_1)}{\sin(\theta_1)} \mathbf{n}$$

The location \mathbf{r}_f on the furnace where the intensity $I_{\lambda,f}(\mathbf{r}_f, \mathbf{s}_f)$ starts off can be determined by tracing in the $-\mathbf{s}_f$ direction from \mathbf{r} once \mathbf{s}_f is determined. In order to obtain the value of $I_{\lambda,f}(\mathbf{r}_f, \mathbf{s}_f)$, we solve for the furnace radiocities in the following enclosure analysis. The furnace wall, the glass interface, and the top and bottom opening disks form an enclosure. In order to make the analysis tractable, the glass outer surface is assumed to be diffuse for radiation exchanges. This assumption does not introduce considerable error since the furnace has a small reflectivity and small view-factors to the glass surface such that the intensities from the glass only contribute a small part of the furnace radiosity. The enclosure is divided into K small elements. The furnace radiosity is given by

$$J_{\lambda,i} = \varepsilon_f E_{b\lambda}(T_f) + (1 - \varepsilon_f) \sum_{j=1}^K J_{\lambda,j} F_{i-j} \quad (17)$$

The radiosity at the glass outer surface is given by (see Fig. 4(b))

$$0 < \lambda < 5 \mu\text{m} \quad J_{\lambda,i} = \int_{\Omega=2\pi, \mathbf{n} \cdot \mathbf{s}_g > 0} [1 - \rho_s(\theta)] \times (n_a/n_g)^2 I_{\lambda,g}(\mathbf{r}, \mathbf{s}_g) \mathbf{n} \cdot \mathbf{s}_g d\Omega + \rho_d \sum_{j=1}^K J_{\lambda,j} F_{i-j} \quad (18)$$

$$\lambda > 5 \mu\text{m} \quad J_{\lambda,i} = \varepsilon_g E_{b\lambda}(T_g) + (1 - \varepsilon_g) \sum_{j=1}^K J_{\lambda,j} F_{i-j} \quad (19)$$

where ε_g is the emissivity of the glass surface; and ρ_d is the diffuse reflectivity at the glass outer surface. Equations (17) to (19) are solved simultaneously, then the incident intensity from the furnace is obtained by

$$I_{\lambda,f}(\mathbf{r}_f, \mathbf{s}_f) = J_{\lambda}(\mathbf{r}_f, \mathbf{s}_f) / \pi \quad (20)$$

3 Results and Discussions

A MATLAB program with C++ subroutines was written to simulate the AMZ (Fig. 1). The same spatial grids are used for solving both the heat equation and the RTE. In order to account for the steep spatial change in the physical variables near the joining interfaces, a grid-refinement study has led to the following scheme: It was found that 155×37 spatial grids (in r and z directions respectively) is sufficient for the simulation, each of which consists of 6×6 control angles for the polar and azimuthal angles respectively. The control angle at the boundary is further divided into 3×3 pixel solid angles to allow for the arbitrary intensity directions after the reflections and refractions at the interfaces.

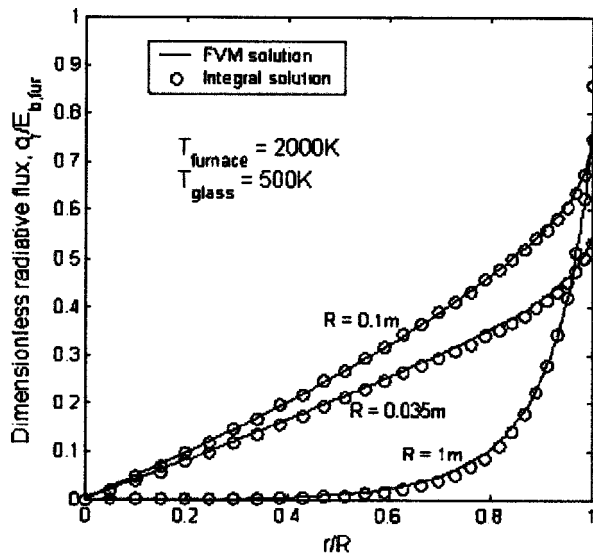
The iterative computation of the intensity begins at the grids adjacent to the boundary surfaces along each specified direction with the guessed boundary intensities and proceeds into the medium. Once the intensities in all the directions are obtained, the linear equations for the radiocities on the K surface elements of the furnace are solved. The boundary intensities at the glass inner surface can now be updated from Eq. (15). The intensities at the gap are also updated from Eq. (14).

The values of (fused silica) glass properties are available in published literature. Specifically, the band model for the spectral absorption coefficient κ_{λ} of the glass is given in Wei et al. [13]. The average refractive index n of glass over the entire spectrum is 1.42. The average glass emissivity at the opaque band is 0.8 (Touloukian et al. [14]). The furnace gray emissivity is 0.75 (Myers [2]).

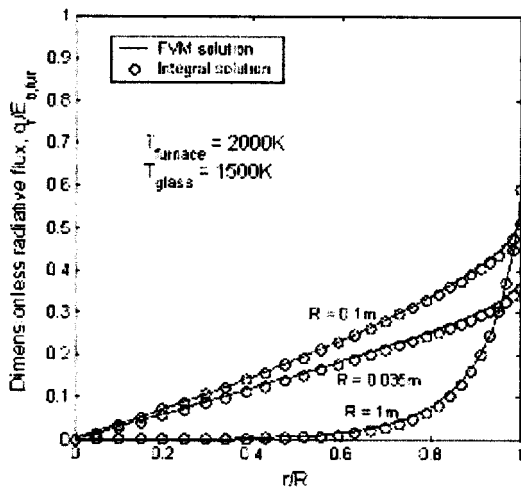
The objectives of the simulations are (1) to validate the numerical model, and (2) to study the effects of the key parameter changes on the temperature distribution during transient. Since direct measurement (temperature or thermal stress) in the preform is extremely difficult, the validation of the model has thus focused on two parts; verification of numerical computation, and qualitative examination of the specular surface assumption against an experimental observation.

3.1 Numerical Validation. Exact integral solution of the RTE is only available for the one-dimensional semitransparent cylinder where the temperature and heat flux only varies in the radial direction (Kesten [15]). In order to validate our 2D solution with this published integral solution, we adapted the boundary conditions to simulate the 1D solution as follows: Both the top and the bottom interfaces of the (constant diameter) cylinder are assumed to be optically smooth with unit reflectivity. In addition, the glass and the furnace wall have uniform temperature such that the radiation intensity does not vary axially. Figure 6 compares the FVM solution and the integral solutions under different glass temperatures and cylinder diameters. The radial flux is normalized to the furnace blackbody emissive power. As shown in Figs. 6(a) and 6(b), the computed results agree well with the exact solutions.

3.2 Qualitative Experimental Verification. In order to examine the specular surface assumption, the temperature distribution during transient was numerically simulated and compared against that with diffuse surfaces. The formulation of the boundary conditions for diffuse surfaces can be found in Jamaluddin and Smith [16] and Yin and Jaluria [9]. The effects of the temperature gradient can then be analyzed qualitatively, and compared against experimental observations. For this study, the glass rod ($L = 0.55$ m) was fed at a constant speed (at 7.5 mm/min) into the



(a)



(b)

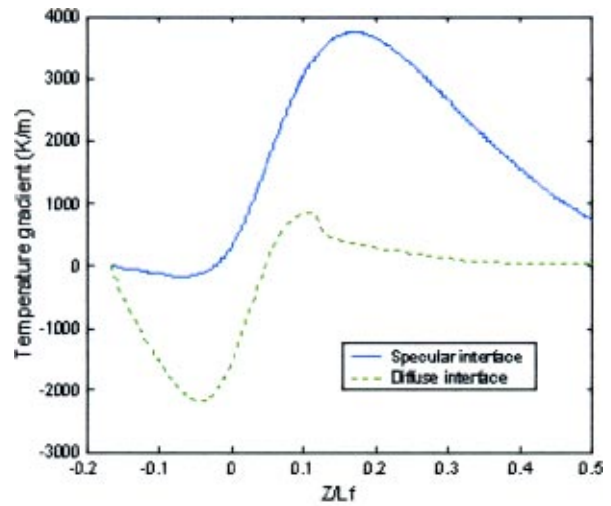
Fig. 6 Comparison of the FVM and the integral solutions: (a) $T_g=500$ K; (b) $T_g=1500$ K

furnace from $Z = -0.16L_f$ to $Z = 0.5L_f$. The rod had an initial temperature of 300K. Other values of the parameters are given in Table 1.

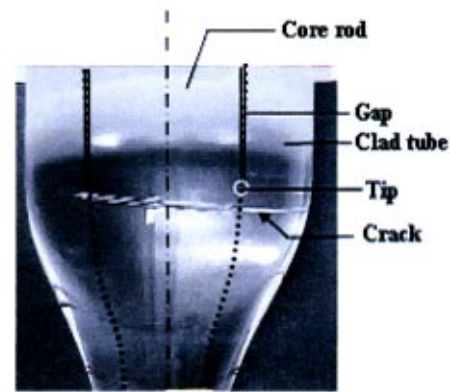
The radial temperature gradients at the tip moved along the axial direction were computed for two different surface assumptions. The results are compared in Fig. 7(a). The diffuse surface preform displays a *negative* maximum-temperature-gradient when most of the preform is still outside the furnace, while the specular surface preform exhibits a *positive* maximum-temperature-gradient in the middle of the feeding process. Since the crack occurs due to the tensile stress developed at the joint tip, a positive radial temperature gradient would make the crack grow outward in the clad tube, while a negative radial temperature gradient

Table 1 Parameters used in the baseline simulation

| R/L | 0.09 | a/R | 0.22 | b/L | 0.14 | c/L | 0.09 |
|--------|------------|---------|------|---------|------|-------------|--------|
| χ | 63° | R/R_f | 0.75 | L_f/L | 0.83 | $T_{f,max}$ | 2400 K |



(a)



(b)

Fig. 7 Effect of temperature gradient on thermal crack: (a) Radial temperature gradient at the tip of the gap; (b) Experimentally observed crack

would make the crack grow inward in the core rod. Experiments showed that when the preform cracks during the AMZ, the crack starts at the joint tip between the core rod and the clad tube and propagates towards the preform surface as illustrated in Fig. 7(b). The fact that the crack grew outward suggests that the specular surface assumption is reasonable in the prediction of the temperature gradient.

To provide a better understanding, the radial temperature distributions around the tip for the two different surface conditions are compared in Fig. 8. The preform temperature with diffuse surfaces increases much faster than that with specular surfaces. For a diffuse interface, the transmitted intensity is uniformly distributed in all the directions regardless of the incident directions and thus a significant part of the incident radiative flux at the surface area outside the furnace is redirected backward to the lower portion of the preform. The relatively high temperature difference between the glass and the environment results in a large heat flux dissipating to the environment through the side surface, which explains the large negative radial temperature gradient when most of the preform is still outside the furnace as shown in Fig. 7(a). As the preform moves further into the furnace, the heat flux from the side surface is balanced somewhat by the conductive flux due to the negative temperature gradient and as a result, the positive gradient is not as high as that in the preform with a specular surface. The abrupt drop of positive temperature gradient in the diffuse surface

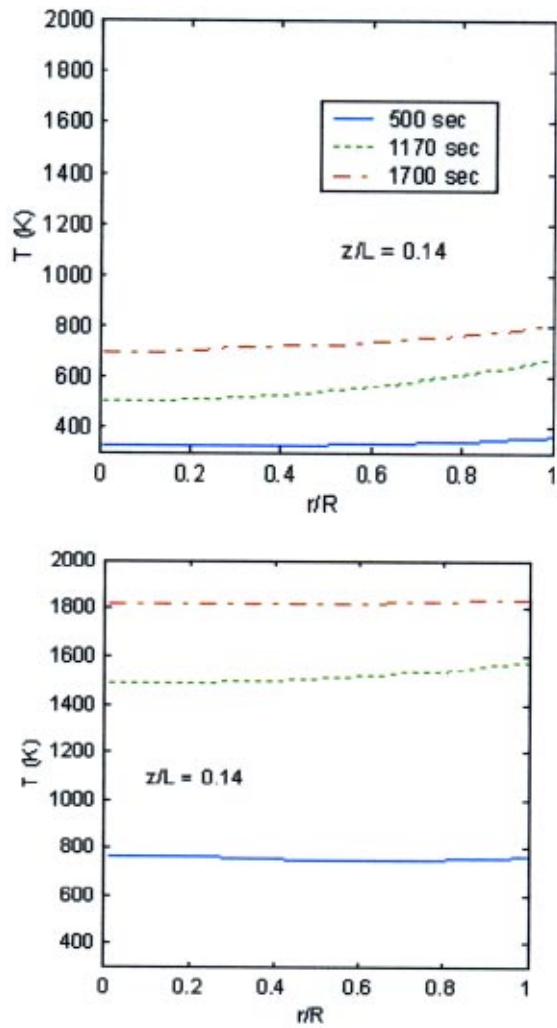


Fig. 8 Comparison of radial temperature distributions: (a) Specular interface; (b) Diffuse interface

perform as shown in Fig. 7(a) is due to the sealing of the gap after the temperature exceeds the softening point of the glass. For a specular surface, the incident ray is refracted in a single direction, and part of the intensity originally from the furnace is reflected from the glass surface into the environment. The preform thus develops a much lower temperature and heat flux. As the specular surface preform has a much lower negative temperature gradient at the beginning of the AMZ, a huge positive temperature gradient is developed as the preform goes further into the furnace.

3.3 Parametric Studies on Temperature Gradient. To reduce the temperature gradient near the tip of the gap without sacrificing the total feeding time, the effects of the following parameter changes on the temperature gradient have been studied numerically:

- | | |
|---|--|
| (1) Baseline simulation: | Table 1 |
| (2) Normalized initial joint length b/L : | 0.08, 0.14 and 0.2 |
| (3) The taper tilt angle χ : | 45°, 63° and 75°; |
| (4) The feed profile: | (a) constant feed rates of 5, 7.5 and 15 mm/min (b) two-stage feed rate |

To aid visualizing how the temperature gradient is developed, the temperature distributions and the divergence of the radiative flux at three instants of time are graphed in Figs. 9 and 10 respectively. In these figures, the axial coordinate begins at the furnace entrance and the negative divergence corresponds to a net inflow of radiative energy into the control volume.

Figure 9 shows a temperature discontinuity at the gap, which has an isolating effect on the heat flux propagation between the two cylinders. The computation of reflectivity in Eq. (13) shows that about only one half of the incident radiative flux is transmitted through the gap from both sides, and the remainder is reflected back. The conductive heat flux is also blocked by the gap but indirectly transferred by the radiative exchange in the opaque band between the two surfaces of the gap. A local peak of radial temperature gradient is developed near the tip due to the temperature discontinuity. When the temperature gradient is greater than some critical value, a crack could develop due to the thermal stress concentration at the tip.

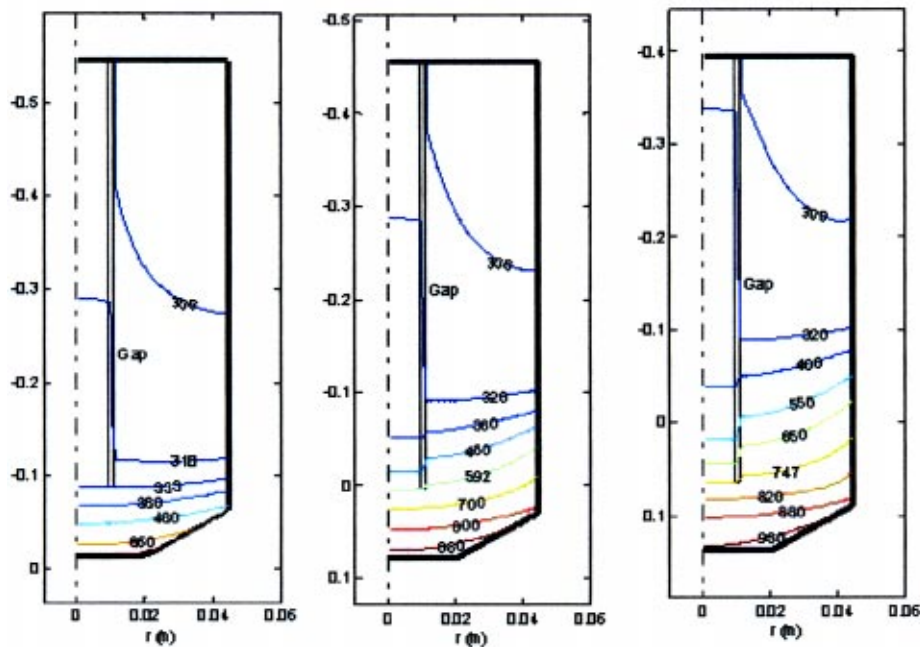


Fig. 9 Temperature contours in the baseline simulation (unit: K): (a) $t=500$ sec, $Z/L_f = -0.03$; (b) $t=1170$ sec, $Z/L_f=0.16$; (c) $t=1700$ sec, $Z/L_f=0.3$

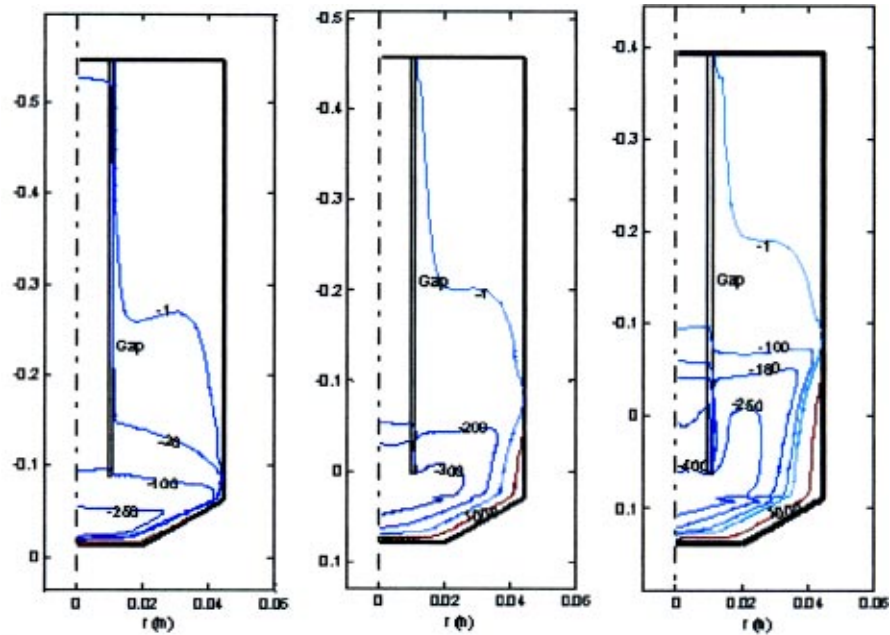


Fig. 10 Contours of the divergence of the radiative flux $\nabla \cdot \mathbf{q}$ in the baseline simulation (unit: kw/m^3): (a) $t=500$ sec, $Z/L_f=-0.03$; (b) $t=1170$ sec, $Z/L_f=0.16$; (c) $t=1700$ sec, $Z/L_f=0.3$

Figure 10 illustrates the divergence of the radiative flux at three different time instants. When the rod is outside the furnace, most of the heat is transferred from the bottom. As shown in Fig. 10(a), the core rod has a higher $\nabla \cdot \mathbf{q}$ since most of the radiative intensities from the bottom are trapped inside the core. On the other hand, the clad tube has a large view-factor to the environment and dissipates heat. Thus, the temperature of the core rod increases at a faster rate and subsequently it is higher than that of the clad tube as shown in Fig. 9(a). Consequently, the radial temperature gradient at the tip is negative. As the rod moves further into the furnace, the heat flux from the furnace through the clad tube becomes larger. This leads to a large positive temperature gradient in the clad tube except the upper region which is still far outside the furnace. Since only a part of the radial heat flux is transferred through the gap, the temperature of the core rod increases at a relatively slow rate, resulting in a positive radial temperature gradient at the tip. Since the glass self emission decreases as the temperature is lower, $\nabla \cdot \mathbf{q}$ in the core rod is larger (in absolute value) than that in the clad tube as shown in Figs. 10(b) and 10(c) as suggested in Eq. (2).

The baseline simulation demonstrated the effectiveness of the numerical model for the prediction and visualization of the temperature field, upon which several methods for reducing the transient temperature gradient were developed. Among these are (1) optimizing the perform design by changing the taper angle χ ; (2) monitoring the length of initial joint, b , during the initial manual fusion process; and (3) mechanically controlling the feed process. The relative effects of these methods are analyzed as follows.

Effects of Geometry. Two geometrical parameters were considered; namely, the initial joint length b and the taper angle χ . The change in b requires additional manual preheating of the perform. Figure 11 shows that an increase or decrease of b has a tendency to increase the magnitude of the maximum temperature gradient. When b is large, the region around the tip is heated mainly by the radial heat flux since the axial heat flux from the bottom is greatly attenuated along the path before reaching the tip. As a result, the temperature of the clad tube is higher than that of the core rod and hence a significantly high radial temperature gradient is developed. When b is small (or that the tip is closer to

the bottom), the clad tube has a larger view factor to the furnace wall than the core rod due to the taper geometry, which results in a higher radial temperature gradient at the tip than that in the baseline case.

Figure 12 shows the temperature gradient decreases with χ . When χ is small, the furnace radiation intensities reaching the taper surface have a smaller incident angle that corresponds to a larger transmittivity. Furthermore, the intensity have a shorter distance to pass through before reaching the tip and thus, it is less attenuated. Consequently, the radial temperature gradient is smaller at the tip.

As shown in Figs. 11 and 12, both of these geometrical parameters have a relatively small effect on the magnitude of the maximum temperature gradient.

Effects of Feed Rate. Two different feed rate control methods for reducing the temperature gradient are discussed here as illustrated in Fig. 13; namely, a constant feed rate and a two-stage feed

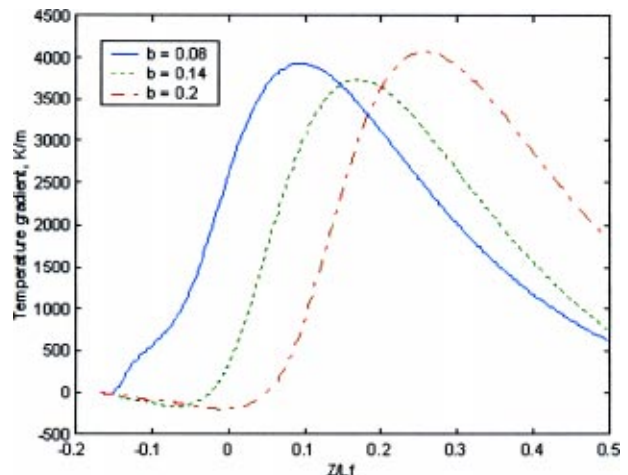


Fig. 11 Effect of initial joint length

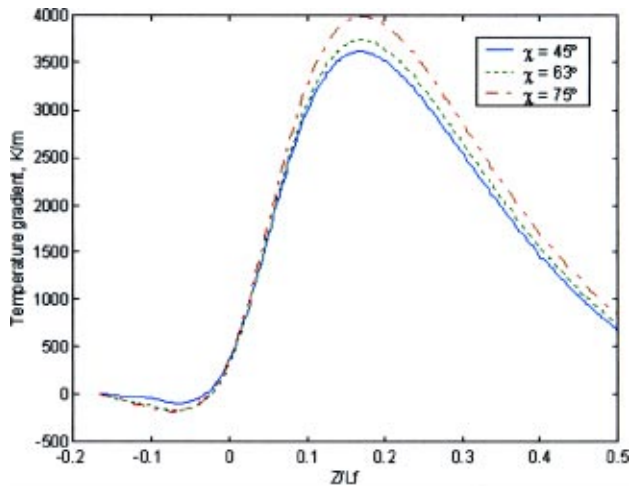


Fig. 12 Effect of taper angle

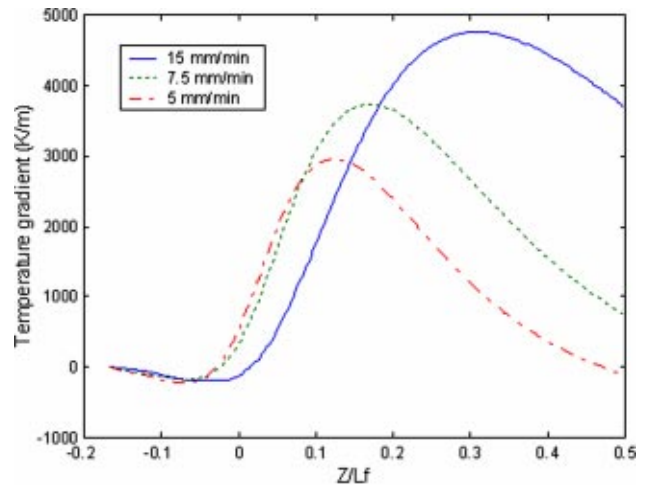


Fig. 14 Effect of feed rate

rate. Figure 14 shows the temperature gradient at the tip, where three different constant feed rates are compared. The maximum temperature gradient decreases as the feed rate decreases since the glass has more time to reduce the gradient through heat transfer. To avoid any crack at the tip, the initial feed rate during the transient must be limited. The tradeoff is that a longer feeding time is needed.

An alternative approach is to use multi-rate feeding control. It can be seen from Fig. 14 that the temperature gradient reaches the maximum and starts to decrease after the glass rod has moved some distance into the furnace. A slower feed rate can be used initially to reduce the maximum temperature gradient followed by faster feed rate to reduce the overall feeding time once the temperature gradient is within an acceptable range. As shown in Fig. 13, the two-stage feed profile takes 32 minutes to feed the glass for the first 40% of the distance while takes only 8 minutes for the rest 60% of the distance. Figure 15 compares the temperature gradients for the two feed profiles in Fig. 13. The result shows that with the two-stage feed profile, the maximum temperature gradient is reduced by about 35% without sacrificing the overall feeding time.

The above studies have suggested that the multi-stage feed rate control is superior in reducing the temperature gradient as com-

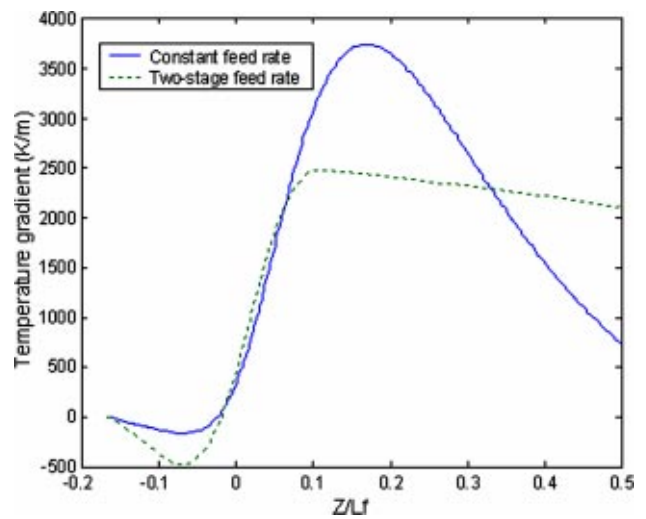


Fig. 15 Comparison of radial temperature gradient at the tip of the gap

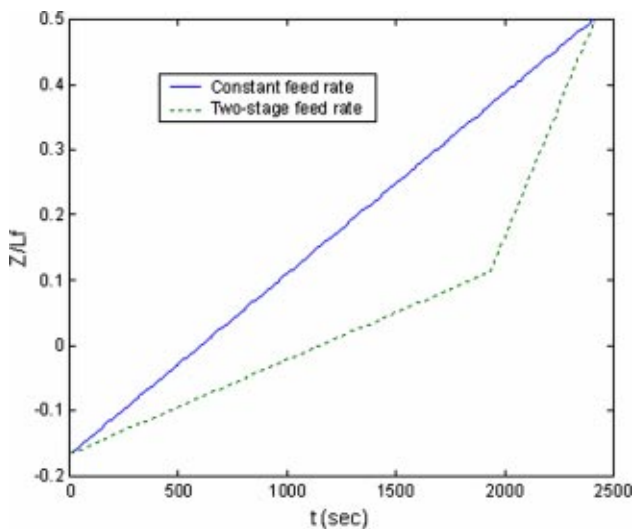


Fig. 13 Different feeding profiles

pared to those focused on geometrical changes. Experiments have been done for the baseline case and the case using the two-stage feed profile (Fig. 13). It was found experimentally that the preform fed at a constant rate cracked in the middle of the process, while the preform fed with multi-rate control did not crack throughout the process.

4 Conclusions

An analytical model has been developed to predict the transient conductive-radiative transfer as two partially joined, concentric glass cylinders are fed into the furnace. The FVM was used to solve the RTE for arbitrary axisymmetric cylindrical geometries with specular interfaces. Transient temperature distribution and its gradient at the tip of the gap are predicted and analyzed under different process parameters.

Our results show that optical conditions at the surface of the preform have a significant effect on the temperature and its gradient during the transient. Preforms with specular surface result in a positive radial temperature gradient near the tip of the gap. Excessive positive radial temperature gradient would lead to thermal crack radially outward. This numerical prediction was found consistent with experimental tests on sample preforms with specu-

lar surfaces. On the other hand, simulation results suggest that negative radial temperature gradient would develop in preforms with diffuse surface at the early stage of the transient.

Parametric studies show that multi-rate preform feeding control can be effectively used to avoid cracks. Specifically, a two-stage control scheme has been tested numerically and experimentally, which shows that an initially slow rate followed by a fast rate can be used to avoid large temperature gradients without significantly sacrifice the overall feeding time. An optimization algorithm can be developed to further reduce the temperature gradient and the feeding time. For a given furnace design and the core/clad diameters, preform geometrical parameters have relatively small effects on the temperature gradient at the tip of the gap.

It is expected that the model and the analysis presented here will serve as a rational basis for design optimization and feed rate control of the process. The computational method of the radiation heat transfer model developed in this paper can also be applied to the simulation of the fiber drawing process and other glass-related manufacturing processes.

Acknowledgments

This research has been funded by OFS (former Lucent Technologies). The authors are deeply indebted to Serge Tchikanda, Steve Jacobs, Rob Moore, and Mahmood Tabaddor for their technical inputs.

Appendix

The RTE for the 2D axisymmetric cylindrical coordinate system is given by Modest [11]:

$$\frac{\alpha}{r} \frac{\partial(rI_\lambda)}{\partial r} - \frac{1}{r} \frac{\partial(\gamma I_\lambda)}{\partial \psi} + \beta \frac{\partial I_\lambda}{\partial z} = \kappa_\lambda [I_{b\lambda}(T) - I_\lambda] \quad (A1)$$

We introduce the relationships among the grid metrics for the general curvilinear transformation [17]: $z_\xi = \eta_r/J$, $-r_\xi = \eta_z/J$, $-z_\eta = \xi_r/J$ and $r_\eta = \xi_z/J$. Noting that $(\alpha z_{\xi\eta} - \beta r_{\xi\eta} - \alpha z_{\xi\eta} + \beta r_{\xi\eta}) = 0$, the 1st and 3rd terms on the left-hand-side of Eq. (A1) can be rewritten as

$$\begin{aligned} & \frac{\alpha}{r} \frac{\partial}{\partial r}(rI_\lambda) + \beta \frac{\partial I_\lambda}{\partial z} + JI_\lambda(\alpha z_{\xi\eta} - \beta r_{\xi\eta} - \alpha z_{\xi\eta} + \beta r_{\xi\eta}) \\ &= \frac{\alpha}{r} \frac{\partial(rI_\lambda)}{\partial r} + \frac{\beta}{r} \frac{\partial(rI_\lambda)}{\partial z} + JI_\lambda \frac{\partial}{\partial \eta}(\alpha z_\xi - \beta r_\xi) \\ & \quad + JI_\lambda \frac{\partial}{\partial \xi}(-\alpha z_\eta + \beta r_\eta) \end{aligned}$$

Upon substituting

$$\begin{aligned} \frac{\partial(rI_\lambda)}{\partial r} &= \frac{\partial(rI_\lambda)}{\partial \eta} \eta_r + \frac{\partial(rI_\lambda)}{\partial \xi} \xi_r, \\ \frac{\partial(rI_\lambda)}{\partial z} &= \frac{\partial(rI_\lambda)}{\partial \eta} \eta_z + \frac{\partial(rI_\lambda)}{\partial \xi} \xi_z \end{aligned}$$

and the grid metrics into the above expression, we have

$$\begin{aligned} \frac{\alpha}{r} \frac{\partial}{\partial r}(rI_\lambda) + \beta \frac{\partial I_\lambda}{\partial z} &= \frac{J}{r} \frac{\partial}{\partial \eta} \left[rI_\lambda \left(\frac{\alpha \eta_r + \beta \eta_z}{J} \right) \right] \\ & \quad + \frac{J}{r} \frac{\partial}{\partial \xi} \left[rI_\lambda \left(\frac{\alpha \xi_r + \beta \xi_z}{J} \right) \right] \quad (A2) \end{aligned}$$

By substituting the above result into Eq. (A1) and then multiplying r/J on both sides of the resulting equation, we obtain Eq. (5). Note that Eq. (5) is in strict conservation form since the grid metrics are inside the differentiations. The advantage of this form is that it satisfies strict energy conservation in the finite volume discretization.

Nomenclature

Capitalized Symbols

- \mathbf{A} = grid face area vector
- C = glass thermal capacity in J/(kg K)
- D = control volume face intensity weight
- E = emissive power in W/(m²)
- F = diffuse view factor
- H = irradiation in W/(m²)
- I = radiative intensity in W/(m² μm sr)
- J = Jacobian of the curvilinear transformation = radiosity in W/(m² μm) in Section 2.2
- L = preform length in m
- L_f = furnace length in m
- R = preform radius in m
- R_f = furnace radius in m
- T = temperature in K
- Z = distance from the entrance of the furnace to the bottom of the preform

Lower-case Symbols

- a = radius of the core
- $a^{mn \pm 1/2}$ = geometric coefficients for face intensities
- b = initial joint length
- c = glass taper length
- d = gap thickness
- k = molecular thermal conductivity in W/(m K)
- n = index of refraction
- \mathbf{n} = normal unit vector of the surface
- \mathbf{q} = total radiative heat flux in W/(m²)
- $q_{rad,opa}$ = radiative flux at the opaque band in W/m²
- \mathbf{r} = position vector
- \mathbf{s} = unit orientation vector of the intensity
- (r, z) = axisymmetric cylindrical coordinates

Greek Symbols

- θ = polar angle of \mathbf{s}
- ψ = azimuthal angle of \mathbf{s}
- Ω = solid angle in sr
- ε = emissivity
- λ = wavelength in μm
- $\eta_r, \eta_z, \xi_r, \xi_z$ = grid metrics
- (η, ξ) = curvilinear coordinates
- ρ = glass density in kg/m³ in Eq. (1)
- = reflectivity in Section 2.2
- κ = absorption coefficient in m⁻¹
- α, β, γ = direction cosines of \mathbf{s}

Superscripts and Subscripts

- a = air in free space
- B = boundary
- e, w, s, n = east, west, south and north side of the control volume
- f = furnace
- g = glass
- m = index of the discrete polar angle
- s = specular
- d = diffuse
- n = index of the discrete azimuthal angle
- M = total number of the polar angles
- N = total number of the azimuthal angles
- λ = wavelength in μm
- b = blackbody
- p = center node of the control volume

References

- [1] Paek, U. C., and Runk, R. B., 1978, "Physical Behavior of the Neck-Down Region During Furnace Drawing of Silica Fibers," *J. Appl. Phys.*, **49**, pp. 4417–4422.

- [2] Myers, M. R., 1989, "A Model for Unsteady Analysis of Preform Drawing," *AIChE J.*, **35**(4), pp. 592–602.
- [3] Xiao, Z., and Kaminski, D. A., 1997, "Flow, Heat Transfer, and Free Surface Shape During the Optical Fiber Drawing Process," *HTD Vol. 347, National Heat Transfer Conference*, Vol. 9, ASME.
- [4] Choudhury, S. R., Jaluria, Y., and Lee, S. H.-K., 1999, "A Computational Method for Generating the Free-Surface Neck-Down Profile for Glass Flow in Optical Fiber Drawing," *Numer. Heat Transfer, Part A*, **35**, pp. 1–24.
- [5] Lee, K. H., and Viskanta, R., 1999, "Comparison of the Diffusion Approximation and the Discrete Ordinates Method for the Investigation of Heat Transfer in Glass," *Glass Science and Technology-Glastechnische Berichte*, **72**(8), pp. 254–265.
- [6] Chai, J. C., Lee, H. S., and Patankar, S. V., 1994, "Finite Volume Method for Radiative Heat Transfer," *J. Thermophys. Heat Transfer*, **8**(3), pp. 419–425.
- [7] Liu, J., Shang, H. M., and Chen, Y. S., 1997, "Prediction of Radiative Transfer in General Body-Fitted Coordinates," *Numer. Heat Transfer, Part B*, **31**(B), pp. 423–439.
- [8] Baek, S. W., and Kim, M. Y., 1997, "Modification of the Discrete-Ordinates Method in an Axisymmetric Cylindrical Geometry," *Numer. Heat Transfer, Part B*, **31**(B), pp. 313–326.
- [9] Yin, Z., and Jaluria, Y., 1997, "Zonal Method to Model Radiative Transfer in an Optical Fiber Drawing Furnace," *J. Heat Transfer*, **119**, pp. 597–603.
- [10] Siegel, R., and Spuckler, C. M., 1992, "Effect of Index of Refraction on Radiation Characteristics in a Heated Absorbing, Emitting, and Scattering Layer," *ASME J. Heat Transfer*, **114**, pp. 781–784.
- [11] Modest, M. F., 1993, *Radiative Heat Transfer*, McGraw-Hill, NY.
- [12] Viskanta, R., and Anderson, E. E., 1975, "Heat Transfer in Semitransparent Solids," *Adv. Heat Transfer*, **11**, pp. 317–441.
- [13] Wei, Z., Lee, K. M., Tehikanda, S. W., Zhou, Z., and Hong, S. P., 2003, "Effects of Radiative Transfer Modeling on Transient Temperature Distribution in Semitransparent Glass Rod," *ASME J. Heat Transfer*, **125**(4), pp. 635–643, Aug.
- [14] Touloukian, Y. S., De Witt, D. P., and Hemicz, R. S., eds., 1973, *Thermal Radiative Properties: Nonmetallic Solids, Vol. 8 of Thermophysical Properties of Matter*, Plenum Press, New York, pp. 1569–1576.
- [15] Kesten, S. Arthur, 1968, "Radiant Heat Flux Distribution in a Cylindrically-Symmetric Nonisothermal Gas With Temperature-Dependent Absorption Coefficient," *J. Quant. Spectrosc. Radiat. Transf.*, **8**, pp. 419–434.
- [16] Jamaluddin, A. S., and Smith, P. J., 1988, "Predicting Radiative Transfer in Axisymmetric Cylindrical Enclosures Using the Discrete Ordinates Method," *Combust. Sci. Technol.*, **62**, pp. 173–186.
- [17] Tannehill, J. C., Anderson, D. A., and Pletcher, R. H., 1997, *Computational Fluid Mechanics and Heat Transfer*, Taylor & Francis.